

Integration over two-dimensional Brillouin zones by adaptive mesh refinement

J. Henk*

Max-Planck-Institut für Mikrostrukturphysik, Weinberg 2, D-06120 Halle (Saale), Germany

(Received 25 January 2001; revised manuscript received 9 April 2001; published 25 June 2001)

Adaptive mesh-refinement (AMR) schemes for integration over two-dimensional Brillouin zones are presented and their properties are investigated in detail. A salient feature of these integration techniques is that the grid of sampling points is automatically adapted to the integrand in such a way that regions with high accuracy demand are sampled with high density, while the other regions are sampled with low density. This adaptation may save a sizable amount of computation time in comparison with those integration methods without mesh refinement. Several AMR schemes for one- and two-dimensional integration are introduced. As an application, the spin-dependent conductance of electronic tunneling through planar junctions is investigated and discussed with regard to Brillouin zone integration.

DOI: 10.1103/PhysRevB.64.035412

PACS number(s): 71.15.Dx, 73.40.Gk, 02.60.Jh

I. INTRODUCTION

The computation of physical quantities often requires integration over the Brillouin zone (BZ). Standard methods to obtain BZ integrals are special-point (SP) schemes¹ and tetrahedron methods.² Since both methods rely on equally spaced grid points, they may be regarded as inefficient if there are small regions in the BZ that give a sizable contribution to the integral, while large regions give almost no contribution: Either the number of grid points may be too small to sample the “important regions” with high accuracy, or the number of grid points may be too high and the “unimportant regions” are sampled with a dispensable high accuracy, thus leading to an unnecessarily large computation time. An integration method that automatically adapts the grid to the integrand’s structure would overcome this problem. Such an adaptive mesh refinement (AMR) would find the important regions with high accuracy demand and sample them with high resolution, while the unimportant regions with low accuracy demand are sampled by a few points. Consequently, discretization on a very fine grid covering the entire BZ is avoided.

Bruno and Ginatempo proposed as an AMR scheme for n -dimensional integrals a cascade of adaptive integration techniques for one-dimensional integrals.³ In this paper, further adaptive integration schemes based on the partitioning of the integration domain by simplexes will be introduced and investigated, with a focus on the computation of physical quantities of layered systems, e.g., the magnetic anisotropy energies of ultrathin films (see Refs. 4 and 5) and magnetoresistances of planar tunnel junctions (for a few recent publications see Refs. 6–9).

Coherent tunneling of electrons through planar magnetic junctions provides a test for the proposed AMR’s. The computation of the spin-dependent conductance requires the integration of the transmission of Bloch electrons through the junction over the two-dimensional BZ. This transmission can depend strongly on \mathbf{k}^{\parallel} (cf. Ref. 10). First, for increasing spacer thickness, the transmission at large $|\mathbf{k}^{\parallel}|$ becomes suppressed, leaving a sizable contribution to the conductance only near the BZ center. Second, electronic states localized at the lead/spacer interfaces can dominate the transmission in

very small regions of the BZ (“hot spots”), not necessarily near the BZ center. In both cases, the regions with high accuracy demand are small in comparison with the area of the BZ and their locations are *a priori* unknown. While special-point schemes appear inefficient, an AMR provides a method of choice since it can efficiently treat both large- and small-scale variations of the integrand.

This paper is organized as follows. After having illustrated the basic idea and the main features of AMR’s by means of one-dimensional integration (Sec. II), adaptive mesh refinements for two-dimensional integration are introduced in Sec. III. Exemplary results for the spin-dependent tunneling conductance for planar junctions are presented in Sec. IV in order to show the properties of the various proposed AMR’s.

II. ADAPTIVE MESH REFINEMENT FOR ONE-DIMENSIONAL INTEGRALS

Adaptive mesh refinements aim to integrate numerically a function $f(x):\mathbb{R}\rightarrow\mathbb{R}$ over the interval $[x_i, x_f]$ with a given accuracy ϵ but with the number $n(\epsilon)$ of function evaluations as small as possible. They rely on three main ingredients:¹¹ (i) a crude approximation $I_{ap}(x_i, x_f)$ to the exact integral $I_{ex}(x_i, x_f) = \int_{x_i}^{x_f} f(x) dx$ [gray area in Fig. 1(a)] that uses only the interval boundaries x_i and x_f , (ii) a fine approximation $I_{ap'}(x_i, x_f)$ that uses (at least) one inner point x_m in addition, and (iii) a refinement rule that in dependence on I_{ap} , $I_{ap'}$, and ϵ determines whether the interval has to be refined.

A crude approximation $I_{ap}(x_i, x_f)$ is for example given by the trapezoidal rule [the area hatched with thin lines in Fig. 1(a)].¹² For a fine approximation $I_{ap'}(x_i, x_f)$, $f(x)$ is integrated by Simpson’s rule, which uses the inner point $x_m = (x_i + x_f)/2$. Instead, one could also use the simpler but less accurate $I_{ap''}(x_i, x_f) = I_{ap}(x_i, x_m) + I_{ap}(x_m, x_f)$ [the area hatched with thick lines in Fig. 1(a)]. The refinement rule states that $I_{ap'}(x_i, x_f)$ is accepted as an approximation for $I_{ex}(x_i, x_f)$ if $|I_{ap'}(x_i, x_f) - I_{ap}(x_i, x_f)| < \epsilon$ (absolute error) or $|I_{ap'}(x_i, x_f) - I_{ap}(x_i, x_f)| < \epsilon |I_{ap'}(x_i, x_f)|$ (relative error). Otherwise the mesh is refined by applying the above scheme to the intervals $[x_i, x_m]$ and $[x_m, x_f]$ [an analog can be for-

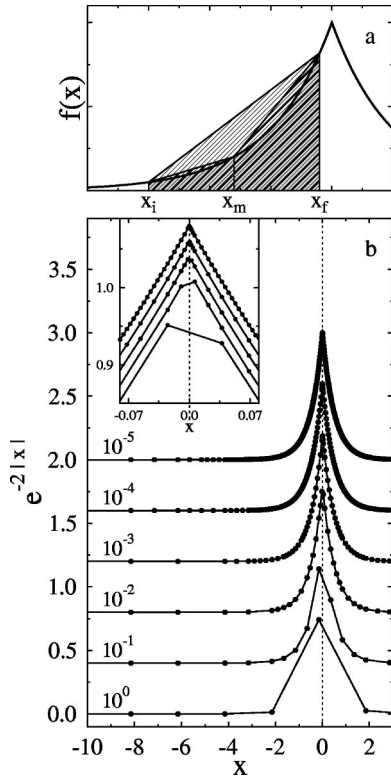


FIG. 1. Adaptive mesh refinement for one-dimensional integrals. (a) The integral of the function $f(x)$ (thick line) over the interval $[x_i, x_f]$ is given by the gray area. A crude approximation uses only x_i and x_f and results in the area hatched with thin lines. A fine approximation uses x_m in addition and leads to the area hatched with thick lines. (b) Adapted meshes $[x, f(x)]$ (dots) of $f(x) = \exp(-2|x|)$ for absolute accuracies ϵ ranging from 10^0 down to 10^{-5} (bottom to top, as indicated on the left of each curve). The inset shows the same data but in a small interval around $x=0$ for $\epsilon=10^{-2}, \dots, 10^{-6}$ (bottom to top). The curves are shifted with respect to each other for clarity. Vertical dashed lines emphasize the mirror symmetry of $f(x)$ at $x=0$.

culated with $I_{ap'}(x_i, x_f)$ instead of $I_{ap}(x_i, x_f)$.

The main properties of this AMR are revealed by considering the function $f(x) = \exp(-2|x|)$ with $I_{ex}(-\infty, \infty) = 1$ [see Fig. 1(b)]. It has been integrated numerically via the above AMR (using trapezoidal and Simpson's rules) from -20.15 to 19.85 with an initial grid of 11 points. (The large interval $[-20.15, 19.85]$ is first partitioned into 10 equally large subintervals which are then treated by the AMR. This initial partitioning determines the large-scale resolution of the adaptive scheme. The small-scale resolution is determined by ϵ .) Whether the AMR is able to recognize the cusp can be tested by choosing the interval asymmetrical with respect to $x=0$. In this case, the cusp is not hit directly by the initial grid and its first refinement. For large $|x|$, $f(x)$ is rather flat and hence I_{ap} and $I_{ap'}$ do not differ significantly. In this unimportant region the demand of accuracy is low and therefore a coarse grid can be maintained. The cusp, however, represents an important region with high accuracy demand and thus requires a fine grid [see the inset in Fig. 1(b)].

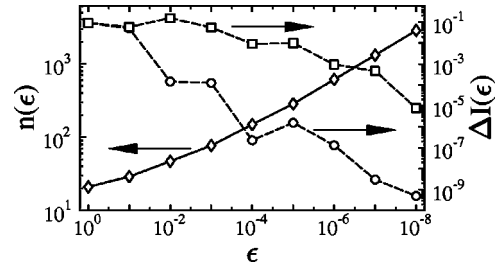


FIG. 2. Numbers $n(\epsilon)$ of mesh points (diamonds) and integration errors $\Delta I(\epsilon)$ (circles) of the AMR for $f(x) = \exp(-2|x|)$ in dependence on the absolute accuracy ϵ . Squares give errors $\Delta I_{ap'}(n(\epsilon))$ of a Simpson integration with the same numbers $n(\epsilon)$ of points as determined by the AMR.

In Fig. 2, the numbers $n(\epsilon)$ of grid points are shown (diamonds). An increase of accuracy by one order of magnitude requires an increase of $n(\epsilon)$ by a factor of about 2.15. The integration error $\Delta I(\epsilon) = |I(\epsilon) - I_{ex}|$ (circles) is always less than ϵ . The efficiency of the AMR becomes evident if one considers the integrals $I_{ap'}(n(\epsilon))$ of $f(x)$ by Simpson's rule with the same number $n(\epsilon)$ of grid points as used by the AMR. For comparably large $n(\epsilon)$, the integration error $\Delta I_{ap'}(n(\epsilon)) = |I_{ap'}(n(\epsilon)) - I_{ex}|$ (squares) is about four orders of magnitude larger than $\Delta I(\epsilon)$. Thus, in order to achieve an accuracy of $\epsilon = 10^{-9}$ in the Simpson integration, a grid of about 32 000 points is needed. This corresponds to an increase in speed by a factor of about 5 in favor of the AMR.

III. ADAPTIVE MESH REFINEMENTS FOR TWO-DIMENSIONAL INTEGRALS

An obvious generalization of the above AMR to integration in n dimensions was proposed by Bruno and Ginatempo.³ The integral $I_{ex}^{(n)} = \int_{[x_i, x_f]} f(x) d^n x$ of $f(x): \mathbb{R}^n \rightarrow \mathbb{R}$ over the interval $[x_i, x_f]$ is decomposed into successive one-dimensional integrals, the AMR of Sec. II being applied to each of them. In a computer program, one would deal with a cascade of AMR's for linear meshes, and hence the name cascading linear mesh refinement, CLMR(n) where n indicates the dimension. To give an explicit example, e.g., a CLMR(2) scheme, for the integral $I_{ex}^{(2)} = \int_{BZ} f(\mathbf{k}^{\parallel}) d^2 \mathbf{k}^{\parallel}$ of the function $f(\mathbf{k}^{\parallel}): \mathbb{R}^2 \rightarrow \mathbb{R}$, $\mathbf{k}^{\parallel} = (k^x, k^y)$, over the two-dimensional BZ $[k_i^{\parallel}, k_f^{\parallel}]$, the cascade is given by $I_{ex}^{(2)} = \int_{k_1^y}^{k_f^y} I_{ex}^{(1)}(k^y) dk^y$, $I_{ex}^{(1)}(k^y) = \int_{k_1^x}^{k_f^x} f(k^x, k^y) dk^x$.

Another type of AMR is based on the refinement of simplexes. A simplex in \mathbb{R}^n is a geometrical object that consists of $n+1$ points and all its constituents (which are themselves simplexes) with dimensions m ($0 \leq m < n$), e.g., corners ($m=0$), line segments ($m=1$), triangular surfaces ($m=2$), etc. Since a simplex is uniquely defined by its corners $\mathbf{x}_1, \mathbf{x}_2, \dots, \mathbf{x}_n, \mathbf{x}_{n+1}$ it can for short be denoted $\langle 1 2 \dots n (n+1) \rangle$. The central point of a simplex, i.e., $\sum_{i=1}^{n+1} \mathbf{x}_i / (n+1)$, will be denoted as $\langle 1 \dots (n+1) \rangle$. For example, the center $\mathbf{x}_4 = (\mathbf{x}_1 + \mathbf{x}_2 + \mathbf{x}_3) / 3$ of a triangle $\langle 1 2 3 \rangle$ can be written as $\langle 4 \rangle = \langle 1 2 3 \rangle$. Further, lengths, areas, or volumes will be written as $|\langle 1 \dots n \rangle|$.

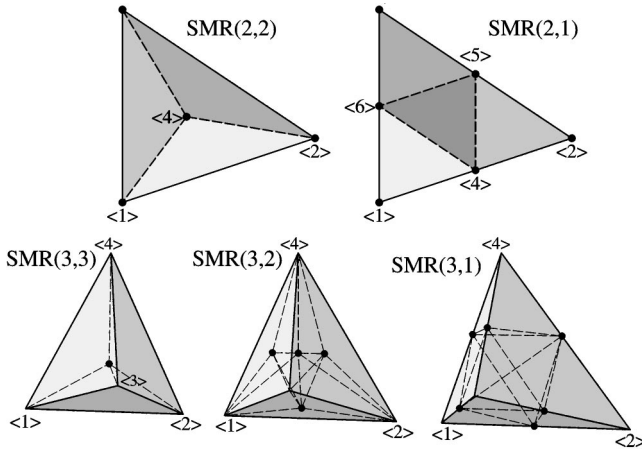


FIG. 3. Simplex mesh refinements $SMR(n,m)$ for triangular ($n=2$, top row) and tetrahedral ($n=3$, bottom row) grids. The mesh refinements are illustrated by dashed lines. Top row: The initial triangle $\langle 1\ 2\ 3 \rangle$ is refined using as additional points the center of the triangle $\langle 4 \rangle$ [left, $SMR(2,2)$] or the edge centers $\langle 4 \rangle$, $\langle 5 \rangle$, and $\langle 6 \rangle$ [right, $SMR(2,1)$]. Bottom row: The initial tetrahedron $\langle 1\ 2\ 3\ 4 \rangle$, with corner $\langle 3 \rangle$ lying behind the front surface $\langle 1\ 2\ 4 \rangle$, is refined using the central point [left, $SMR(3,3)$], the centers of the surfaces [middle, $SMR(3,2)$], or the edge centers [right, $SMR(3,1)$].

Any simplex can be partitioned into smaller simplexes by adding points that are the centers of the m -dimensional constituents of the initial simplex ($1 \leq m \leq n$). These new points in conjunction with the initial points serve as corners of the new (smaller) simplexes, which have to be disjoint and space filling. Consequently, the simplex mesh refinements introduced below can be labeled $SMR(n,m)$.

Suppose we want to integrate numerically a function $f(\mathbf{x}): \mathbb{R}^2 \rightarrow \mathbb{R}$ over a triangle $\langle 1\ 2\ 3 \rangle$. A crude approximation to the exact integral $I_{\text{ex}}(\langle 1\ 2\ 3 \rangle)$ is the volume $I_{\text{ap}}(\langle 1\ 2\ 3 \rangle) = [f(\langle 1 \rangle) + f(\langle 2 \rangle) + f(\langle 3 \rangle)]|\langle 1\ 2\ 3 \rangle|/3$ of the prism. For the mesh refinement $SMR(2,2)$ the center $\langle 4 \rangle = \langle 1\ 2\ 3 \rangle$ is chosen as an additional point (see Fig. 3), and thus $I_{\text{ap}}(\langle 1\ 2\ 3 \rangle) = I_{\text{ap}}(\langle 1\ 2\ 4 \rangle) + I_{\text{ap}}(\langle 2\ 3\ 4 \rangle) + I_{\text{ap}}(\langle 3\ 1\ 4 \rangle)$ is taken as a fine approximation. Or one might utilize for $SMR(2,1)$ the edge centers $\langle 4 \rangle = \langle 1\ 2 \rangle$, $\langle 5 \rangle = \langle 2\ 3 \rangle$, and $\langle 6 \rangle = \langle 3\ 1 \rangle$ with the fine approximation $I_{\text{ap}}(\langle 1\ 2\ 3 \rangle) = I_{\text{ap}}(\langle 1\ 4\ 6 \rangle) + I_{\text{ap}}(\langle 2\ 5\ 4 \rangle) + I_{\text{ap}}(\langle 3\ 6\ 5 \rangle) + I_{\text{ap}}(\langle 4\ 5\ 6 \rangle)$.

As for one-dimensional integration, $I_{\text{ap}}(\langle 1\ 2\ 3 \rangle)$ is accepted in the case of $SMR(2,2)$ if $|I_{\text{ap}}(\langle 1\ 2\ 3 \rangle) - I_{\text{ex}}(\langle 1\ 2\ 3 \rangle)| < \epsilon$ (absolute error) or $|I_{\text{ap}}(\langle 1\ 2\ 3 \rangle) - I_{\text{ex}}(\langle 1\ 2\ 3 \rangle)| < \epsilon |I_{\text{ap}}(\langle 1\ 2\ 3 \rangle)|$ (relative error). Otherwise the AMR is applied to the refined triangles, namely, to $\langle 1\ 2\ 4 \rangle$, $\langle 2\ 3\ 4 \rangle$, and $\langle 3\ 1\ 4 \rangle$. An analog can be formulated for the $SMR(2,1)$ scheme.

It is straightforward to extend the above mesh refinements to three-dimensional integrals (Fig. 3). Using the center of the initial tetrahedron [$SMR(3,3)$] the centers of its four surfaces [$SMR(3,2)$] or the centers of its six edges [$SMR(3,1)$] yield 4, 11, or 8 small tetrahedra, respectively.

Note that the accuracy ϵ is directly related to the integrals over a simplex but only indirectly related to the accuracy of the integral over the complete domain $[\mathbf{x}_i, \mathbf{x}_f]$. In the case of

the refinement rule based on absolute accuracy, the total absolute error can roughly be estimated as $\epsilon N(\epsilon)$ where $N(\epsilon)$ is the number of simplexes used in the evaluation of the integral over the domain.

The AMR schemes are not restricted to integration of real-valued functions. Even matrix-valued functions $f(\mathbf{x}): \mathbb{R}^n \rightarrow \mathbb{R}^{r \times c}$ can be integrated, the integrals being themselves matrices. As a distance in matrix space $\mathbb{R}^{r \times c}$ one could use the matrix norm $\|A\| = \sqrt{\text{tr}(AA^\dagger)}$. An example for operating with matrix-valued functions is a multiple-scattering calculation which takes into account substitutional disorder within the coherent potential approximation.¹³ There, one has to average the scattering-path operator $\tau(E, \mathbf{k})$ over the BZ, the latter being represented in angular-momentum space.¹⁴

IV. APPLICATION TO THE SPIN-DEPENDENT CONDUCTANCE OF PLANAR TUNNEL JUNCTIONS

We now apply the AMR schemes for two-dimensional integration to the computation of the spin-dependent conductance of planar tunnel junctions.⁹ The conductance is calculated for parallel or antiparallel alignment of the magnetic moments of the semi-infinite ferromagnetic leads which are separated by an insulating spacer. If the layer unit cells of the leads and the spacer are commensurate, the in-plane wave vector $\mathbf{k}^{\parallel} = (k^x, k^y)$ is conserved in the scattering process (coherent tunneling). According to Landauer and Büettiker,¹⁵ the conductance G at the Fermi energy can then be expressed as $G = (e^2/h) \int_{\text{BZ}} T(\mathbf{k}^{\parallel}) d^2 \mathbf{k}^{\parallel}$. The transmission is given by $T(\mathbf{k}^{\parallel}) = \sum_{m_L, n_R} |S_{m_L \rightarrow n_R}(\mathbf{k}^{\parallel})|^2$, where S is the scattering matrix of the spacer expressed in terms of lead Bloch states. The sums run over all incoming Bloch states m_L of lead L which are scattered into those outgoing in lead R (n_R). Computation of the conductance by means of a layer Korringa-Kohn-

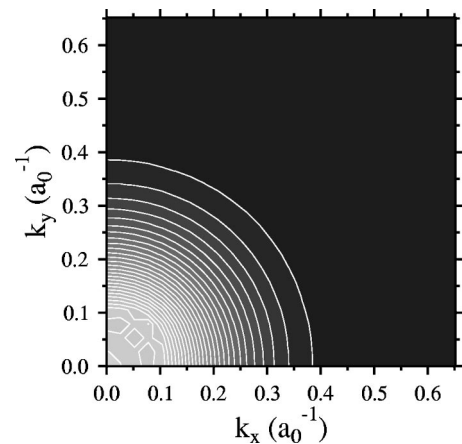


FIG. 4. Transmission $T(\mathbf{k}^{\parallel})$ of Ni(001)/vacuum/Ni(001) for three spacer layers of vacuum and parallel alignment of the lead magnetizations. In the gray-scale contour plot covering one-quarter of the Brillouin zone, zero transmission corresponds to black, while maximum transmission (0.036) corresponds to light gray. Equally spaced contour lines are displayed in white ($\mathbf{k}^{\parallel} = (k^x, k^y)$ with respect to $[\bar{1}10]$ and $[\bar{1}\bar{1}0]$, respectively).

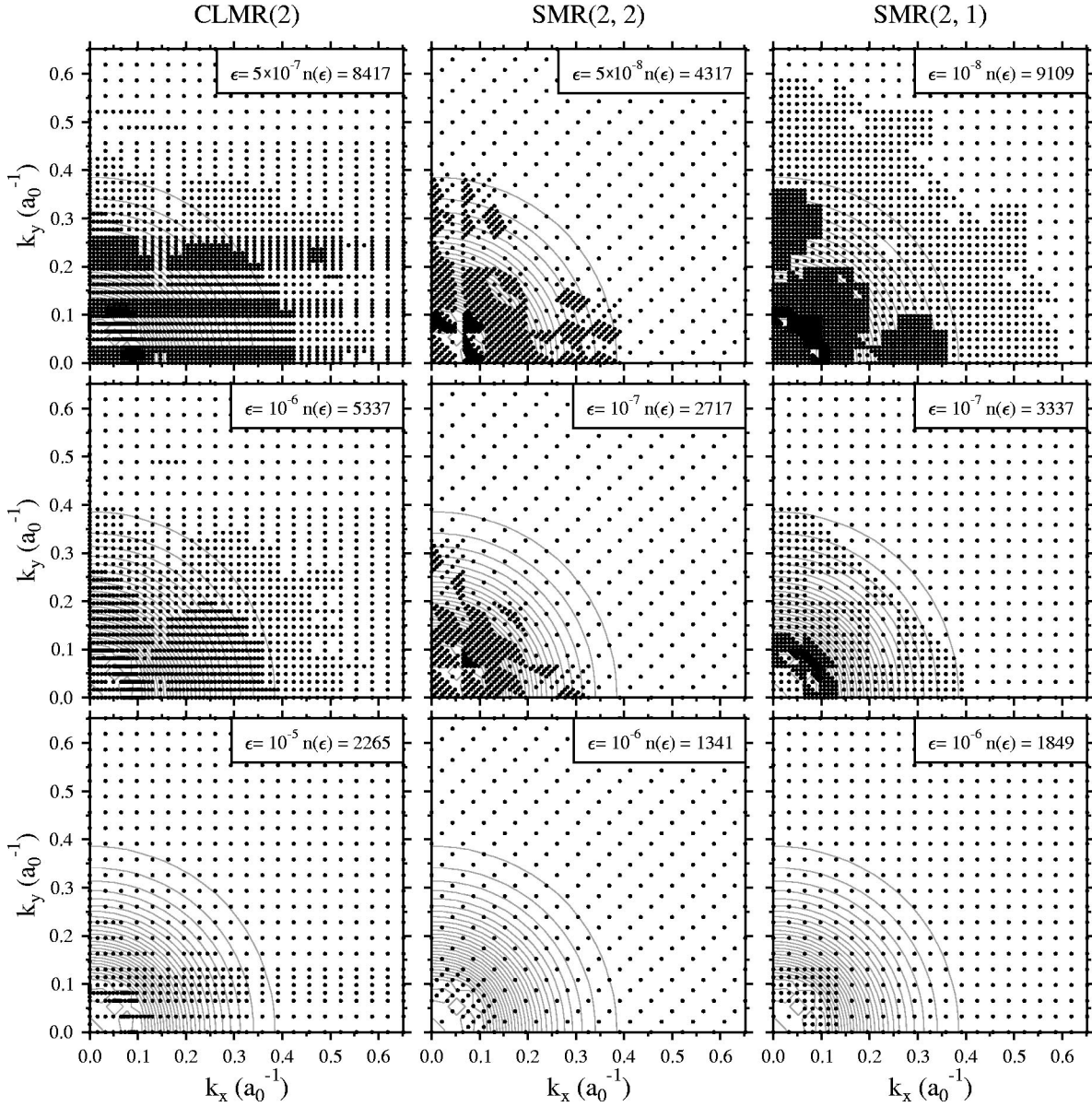


FIG. 5. Adapted meshes (dots) obtained by the CLMR(2) (left column), SMR(2,2) (middle), and SMR(2,1) (right) schemes for the transmission shown in Fig. 4. In the top right corner of each panel, the absolute accuracy ϵ and the number $n(\epsilon)$ of mesh points in the entire Brillouin zone are given. The transmission is displayed in addition by gray contour lines.

Rostoker (KKR) calculation closely follows the work by MacLaren and co-workers.¹⁰

For the purpose of this paper, we focus in the following on the system Ni(001)/vacuum/Ni(001) with the magnetic moments in the leads aligned along the [001] direction. Because $T(\mathbf{k}^{\parallel})$ shows the symmetry of the point group $4mm$, it is sufficient to present results for a quarter of the two-dimensional BZ. The wave vector components k^x and k^y are chosen with respect to [110] and $[\bar{1}10]$, respectively.

Due to the insulating spacer, the conductance G decreases exponentially with spacer thickness. Further, the transmission $T(\mathbf{k}^{\parallel})$ gets focused at the BZ center. For three spacer layers of vacuum and parallel alignment of the lead magnetizations, most of the contributions to G come from the re-

gion with rather small $|\mathbf{k}^{\parallel}|$, say, $|\mathbf{k}^{\parallel}| < 0.25a_0^{-1}$ (Fig. 4). Note that due to the band structure of Ni $T(\mathbf{k}^{\parallel})$ has a plateau-shaped local minimum at $\mathbf{k}^{\parallel} = (0,0)$ which is surrounded by small ‘ridges.’

Adapted meshes obtained by the CLMR(2), SMR(2,2), and SMR(2,1) schemes for selected absolute accuracies ϵ are shown in Fig. 5. The quarter of the BZ was initially partitioned by a 10×10 grid for all three schemes. As expected, the density of mesh points is rather low for small ϵ (bottom row in Fig. 5). A decrease of ϵ leads to a high sampling density of the region with small $|\mathbf{k}^{\parallel}|$, in accordance with the transmission shown in Fig. 4. A slightly increased point density is observed at $|\mathbf{k}^{\parallel}| \approx 0.1a_0^{-1}$, just where the above-mentioned plateau has its boundary. The local minimum at

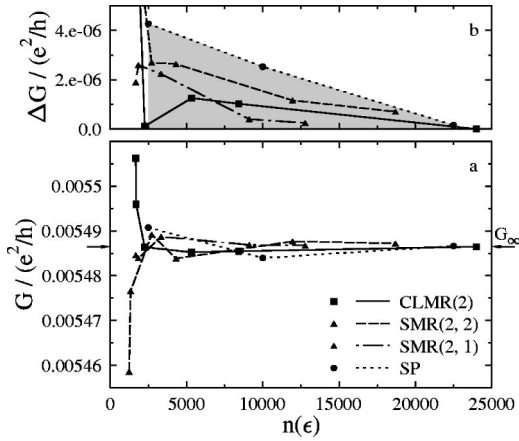


FIG. 6. Conductance G of Ni(001)/vacuum/Ni(001) for three spacer layers of vacuum and parallel alignment of the lead magnetizations in dependence on the number $n(\epsilon)$ of mesh points. (a) Conductance as obtained by the three adaptive mesh refinements CLMR(2) (squares, solid lines), SMR(2,2) (triangles, dashed lines), and SMR(2,1) (triangles, dash-dotted lines), as well as by a special-point scheme (SP, circles, dotted lines). The arrows mark the converged value of the conductance G_∞ . (b) Same data as in (a), but displayed as the absolute deviation from G_∞ , $\Delta G = |G(n(\epsilon)) - G_\infty|$.

the BZ center requires a lower density than the surrounding ridge, as can be seen best for SMR(2,1). In other words, the meshes are adapted to the integrand $T(\mathbf{k}^\parallel)$.

The convergence behavior of the conductance G with decreasing ϵ , and hence increasing number $n(\epsilon)$ of mesh points, is displayed in Fig. 6(a). For small $n(\epsilon)$, the conductance is far from being converged since it shows a significant variation for the CLMR(2) and SMR(2,2) schemes. The SMR(2,1) scheme instead appears to converge faster. For grids of about 5000 to 10 000 points, however, the conductances obtained by all three schemes are almost converged. A further increase of $n(\epsilon)$ reveals that the AMR's are robust, i.e., the conductance shows no considerable oscillations. Since the transmission shows a shape rather similar to that of the function $f(x) = \exp(-2|x|)$ one finds a similar general convergence behavior (cf. Sec. II). The AMR's have been investigated for both a variety of test functions and conductances of other systems (changing lead and spacer materials as well as spacer thicknesses): in all cases, these adaptive integration methods were robust and led to rapid convergence.

In addition to the AMR schemes, the conductance has been calculated with a special-point scheme.¹⁶ The number of mesh points in the entire BZ ranged from 2500 up to 160 000. The conductance G_∞ obtained from the largest number of points represents the converged value of G and can hence be regarded as a reference. For all calculated values, the error $\Delta G = |G(n(\epsilon)) - G_\infty|$ of the AMR's is less than that of the SP scheme, i.e., the AMR points lie within the gray area in Fig. 6(b). Thus, AMR schemes can outperform SP schemes if the integrand shows unimportant regions of considerable size (here, $|\mathbf{k}^\parallel| > 0.3a_0^{-1}$).

A particularly interesting case is tunneling through one

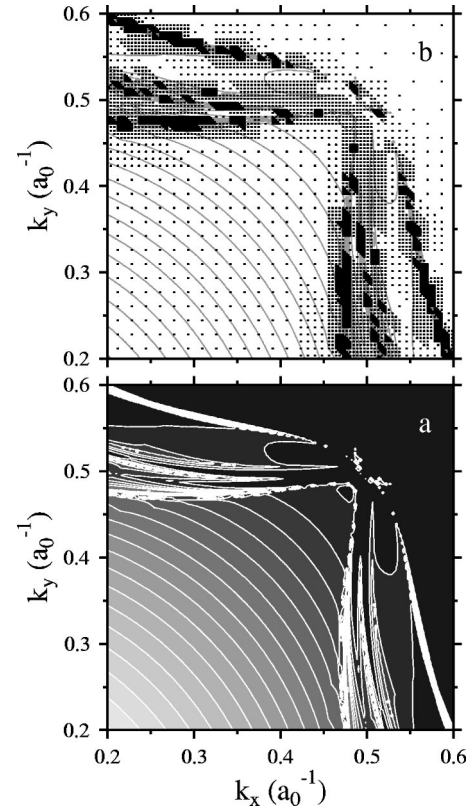


FIG. 7. Transmission $T(\mathbf{k}^\parallel)$ of Ni(001)/vacuum/Ni(001) for one vacuum layer as spacer and antiparallel alignment of the lead magnetizations. (a) $T(\mathbf{k}^\parallel)$ is shown as gray-scale contour, with black for zero transmission and light gray for maximum transmission (0.857). Equally spaced contour lines are displayed in white. (b) Adapted mesh (dots) as obtained by the SMR(2,1) scheme. The contour lines of (a) are shown in gray.

spacer layer for antiparallel alignment of the magnetizations. The transmission for this system decays smoothly with increasing $|\mathbf{k}^\parallel|$, thus leading to a rather large region with almost zero contribution to the conductance [say $|\mathbf{k}^\parallel| > 0.5a_0^{-1}$; black area in Fig. 7(a)]. Consequently, the adapted mesh [Fig. 7(b)] as obtained by SMR(2,1) with $\epsilon = 10^{-6}$ and a 10×10 initial grid is coarse in this area. However, interface resonances produce ‘‘hot ridges’’ with a large transmission (see Sec. I; cf. also Fig. 5 in Ref. 10). The AMR leads to a fine mesh right at these ridges [similar meshes were obtained by both the CLMR(2) and the SMR(2,2) schemes]. This clearly proves that the AMR's discussed in this paper are capable of finding even tiny important regions and therefore may considerably reduce the computation time.

V. CONCLUDING REMARKS

Adaptive mesh-refinement schemes for Brillouin zone integration provide robust numerical methods which automatically find regions with a high accuracy demand. These regions are sampled with high density, while the other regions are sampled with low density. This salient feature may save a considerable amount of computational time as compared to integration methods that rely on equally spaced mesh points,

regardless of the particular AMR used (cascading linear or simplex mesh refinement).

In our computer code for electron spectroscopies which is based on the layer-KKR method, a special-point scheme as well as three AMR's (the cascading linear and two simplex mesh refinements) for integration over the two-dimensional Brillouin zone were implemented. Since it is written in C++, the recursive algorithms of the AMR's could easily be implemented. The nesting is terminated if either the integration error is smaller than the prescribed accuracy or a maximum

recursion level is reached. One minor disadvantage of the AMR's might be that the execution time of a calculation is hard to estimate since the number of mesh points is unknown *a priori*.

Adaptive mesh-refinement schemes, like other grid techniques, are of course not restricted to Brillouin zone integrations (for application of grid techniques in density-functional theory see Ref. 17). We suggest considering the implementation of AMR's in computer codes for electronic-structure calculations.

*Electronic address: henk@mpi-halle.mpg.de

¹R. Evarestov and V. Smirnow, *Phys. Status Solidi B* **119**, 9 (1983).

²P.E. Blöchl, O. Jepsen, and O.K. Andersen, *Phys. Rev. B* **49**, 16 223 (1994).

³E. Bruno and B. Ginatempo, *Phys. Rev. B* **55**, 12 946 (1997).

⁴B. Heinrich and J.F. Cochran, *Adv. Phys.* **42**, 523 (1993).

⁵M. Johnson, P. Bloemen, and J. de Vries, *Rep. Prog. Phys.* **59**, 1409 (1996).

⁶J.C. Slonczewski, *Phys. Rev. B* **39**, 6995 (1989).

⁷E.Y. Tsybal and D.G. Pettifor, *J. Phys.: Condens. Matter* **9**, L411 (1997).

⁸J. Mathon, *Phys. Rev. B* **55**, 960 (1997).

⁹W.H. Butler, X.-G. Zhang, T.C. Schulthess, and J.M. MacLaren,

Phys. Rev. B **63**, 054416 (2001).

¹⁰J.M. MacLaren, X.-G. Zhang, W.H. Butler, and X. Wang, *Phys. Rev. B* **59**, 5470 (1999).

¹¹C.W. Ueberhuber, *Numerical Computation 2* (Springer, Berlin, 1997).

¹²W.H. Press, B.P. Flannery, S.A. Teukolsky, and W.T. Vetterling, *Numerical Recipes. The Art of Scientific Programming* (Cambridge University Press, Cambridge, 1989).

¹³J. Henk, *J. Phys.: Condens. Matter* **13**, 833 (2001).

¹⁴P. Weinberger, *Electron Scattering Theory of Ordered and Disordered Matter* (Clarendon Press, Oxford, 1990).

¹⁵M. Büettiker, *Phys. Rev. Lett.* **57**, 1761 (1986).

¹⁶H.J. Monkhorst and J.D. Pack, *Phys. Rev. B* **13**, 5188 (1976).

¹⁷T.L. Beck, *Rev. Mod. Phys.* **72**, 1041 (2000).